INFN-NSF Summer Exchange Fellowship

A Search for Yet-Undetected Gravitational-Wave Sources

Sara Evangelista
University of Turin
Mentors: Marek Szczepańczyk, Sergey Klimenko
University of Florida
(LIGO Document Control Center: T2400155)

University of Florida
College of Liberal Arts and Sciences
Department of Physics
Gainesville, Florida, USA

August-September, 2023

Contents

Abstract

So far, LIGO and Virgo observed around a hundred gravitational-wave (GW) sources, mostly binary black hole systems. These binaries are characterized by the total mass, a ratio of the component masses, spins, distances, and others. In this report, we studied the properties of these sources and identified the parameter spaces lacking GW detections. We listed examples of the most interesting GW sources that haven't been detected and analyzed their simulated properties and future detectability. Asymmetric binary systems (small ratio of the component masses), for example, are not well covered by the current detections. In our study, we noticed that the amplitude of the GW signal is lower than the symmetric binary systems. For this reason, we expect that more of them will be detected in the future observing runs with improved interferometer sensitivity. Another interesting remark is the fact that the detected GW signals of binaries with low negative spin are similar to those with high positive ones, making it harder to constrain the actual spin value. In particular, this difference is smaller for low-mass binary systems.

1 Introduction

Gravitational wave physics is one of the fundamental ways to learn more about the origin of the Universe and astrophysical phenomena, since GWs carry important information about their source that we have to unveil.

GWs were predicted by Albert Einstein in 1915, as a consequence of his General Relativity theory. Only in 1982 Joseph Taylor Jr. and Russell Alan Hulse provided indirect evidence of their existence by observing a binary system of a pulsar orbiting around a neutron star. Nearly a century after the first prediction, in 2015, the LIGO interferometers detected the signal of the merger of a black hole binary system. Virgo detector joined LIGO two years later and was followed by KAGRA in 2020. We went very far after the first detected gravitational wave signal: today we have detections every few days, and the most up-to-date GWTC includes 90 confident candidates. But there is still a long way to go, for example so far only GWs from binary systems composed of black holes and neutron stars have been detected. In the future, we expect to observe signals from different events, such as supernovae, pulsars or the more exotic cosmic strings.

The purpose of this report is first to study the GWs detected events by looking at their distribution in the parameter space and correlations among parameters, using the data present in the last GWTC. Then we try to predict which kind of events we will probably observe in the near future, which ones are more easily detectable, and what we should prepare for. We focus only on the compact binary systems.

This work is organized as follows: This Section 1 is an introduction to gravitational wave physics and to the detectors' functioning. Section 2 is an overview of the published GWTCs, describing in general the data analysis techniques, the parameters used for describing the sources, and the most significant events detected so far. Section 3 studies the population properties of the already detected events, trying to figure out what trends we can observe and where there is a lack of sources. After, Section 4 analyses examples of interesting binary systems not yet detected, we study the features of their time domain waveform and Amplitude Spectral Density and compare it with the sensitivity curves of the three detectors expected for the fifth observing run (O5). And lastly, in the conclusions, we highlight the most remarkable results obtained.

1.1 General Relativity

General Relativity is the theory of gravitation created by Albert Einstein in 1915 that today helps us to understand most of the gravitational phenomena. It states that our Universe can be described by a four-dimensional grid, with three coordinates for space and one for time, and that the matter can curve and deform the spacetime and the curvature manifests itself through gravity. This is expressed in the *Einstein Equations*, which relate the Riemann tensor of curvature with the mass-energy tensor $T_{\mu\nu}$:

$$R_{\mu\nu} - \frac{1}{2}g_{\mu\nu}R = \frac{8\pi G}{c^4}T_{\mu\nu} = G_{\mu\nu} \tag{1.1}$$

where the quantities used are defined as follows:

$$\text{Riemann Tensor} \quad R^{\lambda}_{\mu k\nu} = \partial_k\Gamma^{\lambda}_{\mu\nu} - \partial_\nu\Gamma^{\lambda}_{\mu k} + \Gamma^{\alpha}_{\mu\nu}\Gamma^{\lambda}_{\alpha k} - \Gamma^{\alpha}_{\mu k}\Gamma^{\lambda}_{\alpha\nu} = -R^{\lambda}_{\mu\nu k} \tag{1.2}$$

$$\text{Ricci Tensor} \quad R_{\mu\nu} = g^{\lambda k}R_{\lambda\mu k\nu} \tag{1.3}$$

$$\text{Ricci Scalar} \quad R = g^{\mu\nu}R_{\mu\nu} \tag{1.4}$$

$$\text{Christoffel symbol} \quad \Gamma^{\lambda}_{\mu\nu} = \frac{1}{2}g^{\lambda\alpha}(\partial_\mu g_{\nu\alpha} + \partial_\nu g_{\mu\alpha} - \partial_\alpha g_{\nu\mu}) \tag{1.5}$$

1.2 Gravitational Waves

Gravitational Waves are one of the possible solutions of the Einstein Equations (EE), they are perturbations of the spacetime that transport energy. Due to the form of EE they are self-interacting.
We will focus only on the weak field regime, far from their sources, where the self-interaction can be neglected and they can be considered as a little variation from the Minkowski metric of a flat space:

$$g_{\mu\nu} = \eta_{\mu\nu} + h_{\mu\nu} \quad \text{with} \quad |h_{\mu\nu}| \ll 1 \tag{1.6}$$

With this approximation we can linearize the EE at the first order of $h_{\mu\nu}$. The result is:

$$G_{\mu\nu} = \frac{1}{2}(\partial_\alpha\partial_\nu h^{\alpha}_{\mu} + \partial_\alpha\partial_\mu h^{\alpha}_{\nu} - \partial_\mu\partial_\nu h - \Box h_{\mu\nu} + \eta_{\mu\nu}(\Box h - \partial_\alpha\partial_\beta h^{\alpha}_{\beta})) \tag{1.7}$$

Now we can simplify this expression defining:

$$\bar{h}_{\mu\nu} = h_{\mu\nu} - \frac{1}{2}\eta_{\mu\nu}h \tag{1.8}$$

and then changing the coordinates we choose the *Lorentz Gauge* for $\bar{h}$:

$$\partial^\nu\bar{h}_{\mu\nu} = 0 \tag{1.9}$$

The final expression in this gauge is the following:

$$\Box\bar{h}_{\mu\nu} = -\frac{16\pi G}{c^4}T_{\mu\nu} \tag{1.10}$$

This is equivalent to choose the *Harmonic Gauge* for h:

$$\partial_\mu h^{\mu}_{\nu} = \frac{1}{2}\partial_\nu h \tag{1.11}$$

If one substitutes this in (1.7) can see that the solution is the same as (1.10). This is true because using the definition 1.8 in the Lorentz gauge gives the harmonic gauge.

Vacuum solution

If one chooses to solve the Einstein Equations in the vacuum, where $T_{\mu\nu} = 0$, they become:

$$\Box \bar{h}_{\mu\nu} = 0 \tag{1.12}$$

This is the D'Alambert wave equation with known solution:

$$\bar{h}_{\mu\nu} = A_{\mu\nu} \cos\left(k_\alpha x^\alpha\right) \tag{1.13}$$

where $k_\alpha = (\omega, \vec{k})$, ω is the angular frequency and $\vec{k}$ is the wave number, related by the dispersion relation. And $A_{\mu\nu}$ is the symmetric polarization tensor, with 10 degrees of freedom. The Lorentz Gauge 1.9, expressed in the Fourier space, leads to the following additional constrain to the amplitude, reducing its degree of freedom to 6.

$$A_{\mu\nu} k^\nu = 0 \tag{1.14}$$

This means that the wavefront is perpendicular to the direction of propagation.

Transverse-Traceless Gauge

Once we have chosen a gauge, we have to make a proper coordinate transformation in order to go into a coordinate system in which the relation (1.9) is valid. In the previous case we have:

$$x'^\mu = x^\mu + \xi^\mu \tag{1.15}$$

where we assume that $|\partial_\nu \xi^\mu| \ll 1$, and we have the freedom to choose ξ in the gauge:

$$\xi^\mu = B^\mu \cos k_\alpha x^\alpha \tag{1.16}$$

Since now B^μ is still to be defined but we can use it to new relations for the amplitude $A_{\mu\nu}$. The new constraints called *The Transverse-Traceless Gauge* (TT gauge) are:

$$A^\mu_\mu = 0 \tag{1.17}$$

$$A_{\mu\nu} U^\nu = 0 \tag{1.18}$$

These reduce further the degrees of freedom of $A_{\mu\nu}$ from 6 to 2.
U^μ is an unconstrained four-vector that for us represents the four-velocity and we define in the easiest way as $U^\mu = (1, 0, 0, 0)$, imposing that the wave is propagating in the z-direction. Applying all these conditions, that are five but one is redundant, the wave propagating in the z direction become:

$$h^{TT}_{\mu\nu} = \begin{pmatrix} 0 & 0 & 0 & 0 \\ 0 & h_{xx} & h_{xy} & 0 \\ 0 & h_{xy} & -h_{xx} & 0 \\ 0 & 0 & 0 & 0 \end{pmatrix} \tag{1.19}$$

where the independent parameters are two as expected.

Interaction with Matter

Let us consider two free-falling particles with coordinates x^μ and $x^\mu + \zeta^\mu$. The equation of the separation of the geodesics is:

$$\frac{D^2\zeta^\rho}{D\tau^2} = R^\rho_{\lambda\nu\mu}\zeta^\lambda u^\mu u^\nu \tag{1.20}$$

where u^μ is again the four velocity. In the slow motion approximation $\frac{dx^i}{d\tau} \ll \frac{dx^0}{d\tau}$ and $\tau \sim t$, so we can disregard the spatial term and the velocity becomes $u^\mu = (u^0, 0, 0, 0)$. Being in the free-falling approximation we can also consider $\Gamma^\mu_{\nu\lambda} = 0$ and the previous equation become:

$$\frac{d^2\zeta^\rho}{d\tau^2} = R^\rho_{0\lambda 0}\zeta^\lambda c^2 \tag{1.21}$$

in the weak field approximetion and in the TT gauge it becomes:

$$\ddot{\zeta_\mu} = \frac{1}{2}\ddot{h}^{TT}_{\mu\nu}\zeta^\nu \tag{1.22}$$

It shows that perturbations lay just in the directions perpendicular to the propagation. In the time direction and propagation direction there is no deformation due to the gravitational waves.

Polarisation

We can rewrite the notation (1.19) defining the two polarisation states at $z = 0$, choosing $h_{ij} = 0$ when $t = 0$:

$$h_{xx} = h_+ \sin\omega t \quad \textit{Plus polarization} \tag{1.23}$$

$$h_{xy} = h_\times \sin\omega t \quad \textit{Cross polarization} \tag{1.24}$$

Let us divide then the wave into the two components and to study them one at the time. The first one becomes:

$$h^{TT}_{\mu\nu} = h_+ \sin\omega t \begin{pmatrix} 0 & 0 & 0 & 0 \\ 0 & 1 & 0 & 0 \\ 0 & 0 & -1 & 0 \\ 0 & 0 & 0 & 0 \end{pmatrix} \tag{1.25}$$

We will consider now two particles laying on the plane (x, y) orthogonal to the propagation direction. Their coordinates are $(0, 0)$ and

$$\vec{\zeta} = (x_0 + \delta x(t), y_0 + \delta y(t)) \tag{1.26}$$

accordingly with the previous definition. Where (x_0, y_0) is the fixed and unperturbated position of the second particle, that changes with the passage of the GW. Both particles are moving on geodesics, so we can substitute the coordinates in the equation (1.22) which describe the variation of the distance of the two particles. We will get:

$$\begin{cases} \delta\ddot{x} = -\dfrac{1}{2}h_+(x_0 + \delta x(t))\omega^2 \sin\omega t \\ \delta\ddot{y} = \dfrac{1}{2}h_+(y_0 + \delta y(t))\omega^2 \sin\omega t \end{cases} \tag{1.27}$$

If we consider a small perturbation we can disregard the perturbative terms $(\delta x(t), \delta y(t))$. Intergrating the equations we will get:

$$\begin{cases} \delta x = \dfrac{1}{2} h_+ x_0 \sin \omega t \\ \delta y = \dfrac{1}{2} h_+ y_0 \sin \omega t \end{cases} \tag{1.28}$$

Similarly if we consider the other component:

$$h_{\mu\nu}^{TT} = h_\times \sin \omega t \begin{pmatrix} 0 & 0 & 0 & 0 \\ 0 & 0 & 1 & 0 \\ 0 & 1 & 0 & 0 \\ 0 & 0 & 0 & 0 \end{pmatrix} \tag{1.29}$$

and we find, after doing all the calculations:

$$\begin{cases} \delta x = \dfrac{1}{2} h_\times y_0 \sin \omega t \\ \delta y = \dfrac{1}{2} h_\times x_0 \sin \omega t \end{cases} \tag{1.30}$$

If we consider a ring of particles, we can see that it behaves differently if the wave that passes through in the perpendicular direction has one polarization or the other. Particularly this is shown in the Figures 1 and 2.

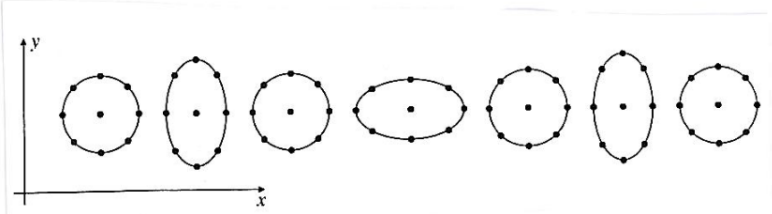

Figure 1: Ring of particles interacting with a plus polarised GW

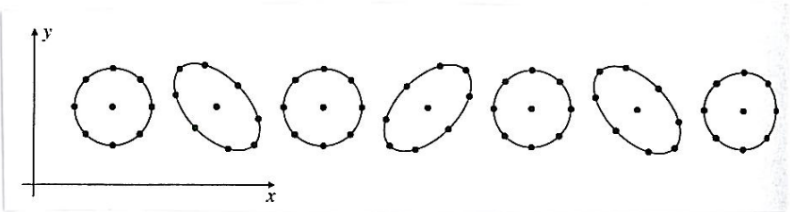

Figure 2: Ring of particles interacting with a cross polarised GW

GW Production

Now we can consider the GW linearised equation (1.10) in presence of a source:

$$\left(-\frac{\partial^2}{\partial t^2} + \nabla^2 \right) \bar{h}_{\mu\nu} = -\frac{16\pi G}{c^4} T_{\mu\nu} \tag{1.31}$$

This expression can be reversed using the Green function formalism, the results is:

$$\bar{h}_{\mu\nu}(t, \vec{x}) = -\frac{16\pi G}{c^4} \int G(x - y) T_{\mu\nu}(y) d^4 y \tag{1.32}$$

where the retarded Green function G in defined as follow:

$$\Box_x G(x-y) = \delta^{(4)}(x-y) \tag{1.33}$$

from which

$$G(x-y) = -\frac{1}{4\pi|\vec{x}-\vec{y}|}\delta\left(|\vec{x}-\vec{y}| - (x^0-y^0)\right)\theta(x^0-y^0) \tag{1.34}$$

Integrating on the time coordinate and using a Dirac delta we will get:

$$\bar{h}_{\mu\nu}(t,\vec{x}) = \frac{4G}{c^2}\int \frac{T_{\mu\nu}(t-|\vec{x}-\vec{y}|/c,\vec{y})}{|\vec{x}-\vec{y}|}d^3y \tag{1.35}$$

it represents the integral on all the points y in space of the source, which has an influence on the point x that I am studying.

Quadrupole momentum

As we said $T_{\mu\nu}$ is the stress-energy tensor, and it has to satisfy the energy-momentum conservation:

$$\partial_\nu T^{\mu\nu} = 0 \tag{1.36}$$

which implies the mometum constance

$$\int T_{\mu 0} d^3y = P_\mu = const \tag{1.37}$$

and also $h_\mu 0 = const$. Let us also introduce a new quantity, the quadrupole momentum:

$$I^{kl} = \int T^{00} y^k y^l d^3y \tag{1.38}$$

where T^{00} is the mass-density.
Moreover from the 1.36 we can derive the following identity:

$$\frac{\partial^2}{\partial t^2}\int T^{00} y^k y^l d^3y = 2\int T^{kl} d^3y \tag{1.39}$$

that can be used to obtain the final form:

$$\bar{h}_{ij} = \frac{2G}{c^2 r}\ddot{I}_{ij}(t-r/c) \tag{1.40}$$

This said that a gravitational wave is produced if the second time derivative of the quadrupole moment of the source is non zero.

1.3 Detectors

One of the first who tried to detect a GW was Joseph Weber in the '60s using bar detectors, which are cylinders with a resonant frequency. But this technique was not as precise as others proposed later on.
In particular the most promising one was the Interferometric Technique used by Michelson in the previous century. It was already used in the well-known Michelson-Morley experiment, which negated the presence of aether giving the basis for the Special Relativity. Proposed in the '60s and '70s, and successively improved, laser

interferometers for the detection of GWs have been built in some locations all over the world and lead to the first detection of a Gravitational Wave in 2015. The most important built nowadays are VIRGO in Italy, LIGO in the USA, and KAGRA in Japan.

Michelson Interferometer functioning

Interferometers are detectors that use light interference to extract information. They consist of laser sources separated by a beamsplitter in two perpendicular arms. After reflecting by two mirrors it merges and interacts with a photodiode. A schematic representation can be seen in Figure. It measures the relative difference in length of the two arms through the interference fringe, connecting it to the strain $h(t)$ in the following way:

$$\delta L(t) = \delta L_x - \delta L_y = h(t)L \tag{1.41}$$

where δL_x and δL_y are the variations of the two arms independently and $L_x \quad L_y \quad L$- This formula can be derived from theory.

Modern interferometers

Modern GW interferometers like Virgo and LIGO are improved and modified versions of the original Michelson interferometer. Some of the most important advancements are:

1. Resonant optical cavities (Febry-Perot cavities): they are used to extend the length of the arms, thanks to mirrors reflecting light up to 300 times

2. Power recycling cavities: mirrors that reflect the light reflected back in the direction of the source by the beamsplitter

3. Signal recycling cavities: they serve to enhance the precision of the final signal

The signal is never pure, there is always some noise. The source of the noise is various and generally, it depends on the frequency range. For example, at high frequencies, it dominates the *photon shot noise*, which can be reduced by increasing the power in the arms. On the other hand, at low frequencies, the interferometer is mainly limited by *seismic noise*, a displacement noise caused by the motion of the ground. Some systems are necessary, such as seismic isolation, to suppress the noise. Instead in the intermediate frequencies, there is *thermal noise* and the problem of scattered light.

Antenna patterns

The GW detectors measure the variation of the length of their arms, so the sensitivity depends on the relative orientation of the arms with respect to the arrival direction of the GW. This spatial sensitivity is called *Antenna pattern* and it changes with the shape of the detector. Most of them have an L-shape, with two perpendicular arms, but it has recently proposed a V-shape for future detectors such as the Einstein Telescope. The sensitivity can also change over time, and this is due to many factors, among which is the Earth's rotation.

L-shape detectors

Let's consider an L-shape detector with equal arms, each one corresponding respectively to the x-axis and y-axis, the center in the beamsplitter, and the direction of propagation of the GW along the z-axis. When a GW is passing the movements of the detector mirrors is described by:

$$\ddot{\zeta}_A^i = -\frac{1}{2}\ddot{h}_{ij}^{TT}\zeta_A^i \tag{1.42}$$

Where $A = 1, 2$ corresponds to the two mirrors. If we neglect the movement in the direction perpendicular to the arm itself we have:

$$\begin{aligned} \delta\vec{\zeta_1} &= (\zeta_1^x, \zeta_1^y) = (L + \delta\zeta_1^x, 0) \\ \delta\vec{\zeta_2} &= (\zeta_2^x, \zeta_2^y) = (0, L + \delta\zeta_2^x) \end{aligned} \tag{1.43}$$

Substituting these in (1.42) we obtain:

$$\begin{cases} \delta\ddot{\zeta}_1^x = \frac{1}{2}\ddot{h}_{xx}(L + \delta\zeta_1^x) \\ \delta\ddot{\zeta}_2^x = \frac{1}{2}\ddot{h}_{yy}(L + \delta\zeta_2^x) \end{cases} \tag{1.44}$$

If we assume a monochromatic wave $h_{ij} = A_{ij}\cos(\omega t)$ we get:

$$\begin{cases} \delta\ddot{\zeta}_1^x = -\frac{1}{2}A_{xx}(L + \delta\zeta_1^x)\omega^2\cos(\omega t) \\ \delta\ddot{\zeta}_2^x = -\frac{1}{2}A_{yy}(L + \delta\zeta_2^x)\omega^2\cos(\omega t) \end{cases} \tag{1.45}$$

and then solving the system in the hypotesis that $\delta\zeta_A^1 \ll L$ we finally arrives at:

$$\begin{cases} L_x = \zeta_1^x = \frac{1}{2}A_{xx}L\cos(\omega t) = \frac{1}{2}h_{xx}L \\ L_y = \zeta_2^y = \frac{1}{2}A_{yy}L\cos(\omega t) = \frac{1}{2}h_{yy}L \end{cases} \tag{1.46}$$

Since $h(t) = \frac{L_x - L_y}{L}$ the strains become:

$$h(t) = \frac{(L + \delta\zeta_1^x) - (L + \delta\zeta_2^y)}{L} = \frac{1}{2}(h_{xx} - h_{yy}) \tag{1.47}$$

This equation can be generalised as follow:

$$h(t) = \frac{1}{2}n_1(\tilde{h}\cdot n_1) - \frac{1}{2}n_2(\tilde{h}\cdot n_2) \tag{1.48}$$

where n_1 and n_2 are the unit vectors along the arms of the detector, and h is the strain in the detector frame.
In general the strain can always be written as a combination of the polarisation states and the antenna patterns F_+ and $F_\times$:

$$h = F_+h_+(t) + F_\times h_\times(t) \tag{1.49}$$

They depend on the shape of the detector and on the position in the sky. With an L-shape detector and a gravitational wave arriving from (θ, ϕ) with polarisation ψ they can be written:

$$\begin{aligned} F_+ &= \frac{1}{2}(1 + \cos^2(\theta))\cos(2\phi)\cos(2\psi) - cos(\theta)\sin(2\phi)\sin(2\psi) \\ F_\times &= \frac{1}{2}(1 + \cos^2(\theta))\cos(2\phi)\sin(2\psi) + cos(\theta)\sin(2\phi)\cos(2\psi) \end{aligned} \tag{1.50}$$

2 Gravitational Wave Transient Catalogs

There are currently four detectors in the global network of Advanced gravitational-wave detectors, the two of LIGO, Virgo, and KAGRA. Since the first observation of a gravitational-wave source in 2015 (GW150914) we have witnessed three observing runs, and the fourth is still ongoing (O4). From time to time has been published a catalog (known as GWTC or Gravitational-Wave Transient Catalog) with all the confidently detected sources of the previous runs. The GWTCs we have up to now are four:

- **GWTC-1**: The first one covers the first and second observing runs (O1-O2) that took place between September 2015 and August 2017, during which the VIRGO detectors joined LIGO just for the last part of O2. It reports the detection of one binary neutron star event (GW170817) and 10 binary black hole events. [7]

- **GWTC-2**: The second catalog refers to the first part of the third run (O3a) of LIGO and Virgo. It added 39 sources to the previous already listed, which spans a very wide range of parameters and different sources, binary black holes (BBH), binary neutron stars (BNS), and neutron star black holes (NSBH) [8]

- **GWTC-2.1**: This catalog updates the previous one, covering again to the period O3a but including events with a lower statistical significance, due to some improvements in the data analysis techniques. In particular, it is helpful for multimessenger research. [9]

- **GWTC-3**: This last catalog collects the events from the second half of the third run (O3b) which lasted from November 2019 to March 2020. It adds a total of 35 new sources, so the total number of events observed today is 90. In this observing run, KAGRA joined LIGO and VIRGO for the first time. [11]

Note that the name convention to label each candidate is a prefix "GW" followed by the date of the detection (i.e. GW150914), successively updated adding also the UTC time of the detection in order to discern two events detected the same day (i.e. GW190701_203306).

2.1 Data analysis techniques

The search for a gravitational wave signal in the detected data is carried out with two different and complementary techniques. The first one is called "matched filtering" which compares templates, which are simulated theoretical signals from potential sources, with the detected data trying to find a match. The algorithms that use this method are *PyCBC*, *MBTA*, and *GstLAL*. On the other hand, there is the "Minimally modeled search" that does not look for a specific signal form, but it needs the same signal to be detected in at least two detectors to be identified. The algorithm used for this method is *cWB* [3]. Although the templates method is easier for identifying the signal, the minimally modeled technique ensures that nothing is missed just because we lack a theoretical model.

The algorithms determine the likelihood that each candidate is simply terrestrial in origin (noise) or has an astrophysical origin (p-astro). Other important parameters are the SNR (signal-to-noise ratio), which is the strength of the signal with respect to the noise, and the statistical significance or FAR (false alarm rate), which quantifies the rate one can expect that candidate to occur.

2.2 Properties

Once identified the GW signal is possible to infer from the data an estimate of the source physical parameters, which can be divided into two classes: intrinsic and extrinsic. The former are properties of the system itself, for black holes generally are the mass, the spin, and the electric charge, but we assume to neglect the electric charge [7]. Instead the latter is related to how it is observed from the Earth, like the distance, the position in the sky, the phase, and the time of the merging. [10] Since neutron stars are made of matter they have also a parameter for deformability known as "tidal deformability".

Studying the properties of these objects is very important to learn how the binaries formed. [10] The main parameters we will take into consideration are the ones described below.

Mass

The mass is the best-constrained parameter in a binary system. In particular, we are most interested in the mass of each component, assuming that $m_1 > m_2$ and the total mass is defined as $M = m_1 + m_2$. We typically use a cutoff at $3\,\mathrm{M}_\odot$ between the masses of black holes and neutron stars, to distinguish the three kinds of binaries (BH, NS, and NSBH) but the maximum upper mass for NS is currently uncertain. For this reason, we divide the sources into unambiguous BBHs and potential NSs systems. [11]

Another interesting parameter, that is much harder to constrain is the mass ratio:

$$q = \frac{m_1}{m_2} \leq 1 \tag{2.1}$$

Most of the binaries we have measured present a mass ratio close to one, but there are some cases of strong asymmetry.

Chirp mass

The signal measured before the merger, during the "inspiral" phase, is dominated by the chirp mass, a specific combination of the two masses of the components. It is defined as follows:

$$\mathcal{M} = \frac{(m_1 m_2)^{3/5}}{(m_1 + m_2)^{1/5}} = \frac{q^{3/5}}{(1+q)^{6/5}} \tag{2.2}$$

This is also the best-measured parameter for low-mass binary systems and it is better constrained than the individual component masses.[5]

Effective spin

The spin can reveal important information about the evolutionary history of the binary, however, with current detector sensitivity, it is difficult to estimate the individual spin. An easier spin-related parameter to constrain is the "effective aligned spin", defined as a mass-weighted combination of the spins of the compact object before they merge:

$$\chi_{eff} = \frac{(m_1 \vec{\chi}_1 + m_2 \vec{\chi}_2) \cdot \vec{L}_N}{M} \tag{2.3}$$

where $\vec{L}_N$ is the unit vector along the Newtonian orbital angular momentum, and it depends of the tilt angle between the single components and the binary orbit. For example, negative spin indicates misaligned spins. [7] In some cases, in binaries with q close to unity, is possible to better constrain the individual spin of the more massive component. [8]

We can also use an "effective precession spin" χ_p parameter to take account of the precession of the orbital plane of the binary. Also in this case precession is better constrained in the case of unequal mass binaries and precession is maximally visible in the case of edge-on binaries. [13] So far we have just one case of a system with mild evidence of precession. [8]

Distance

Since the amplitude of the signal is inversely proportional to the distance of the source, we can infer the Luminosity Distance of the binary system. Using a flat ΛCDM cosmology model with Hubble constant $H_0 = 67.9\,\mathrm{km\,s^{-1}Mpc^{-1}}$ and matter density $\Omega_m = 0.3065$ we can calculate the redshift [8]. The furthest event detected so far is GW190403_051519 in the second catalog with z = 1.18.

Inclination Angle

In general, the inclination angle between the line of sight and the total angular momentum is only weakly constrained, and for most events, it has a distribution consistent with a source either face on ($\theta_{JN} = 0°$) or face off ($\theta_{JN} = 180°$). These orientations produce the greatest gravitational wave amplitude, and so the binaries can be seen from a larger distance. [6] The only case of a source with a different angle is GW170818, from the GWTC-1, with $45° < \theta_{JN} < 135°$.
In the third catalog we have two sources that can be classified as edge-on binaries (GW20012_06545 and GW191219_16312), but the result is uncertain and it depends on the theoretical model used for the parameter estimation.

2.3 Special events

In each catalog there are some more remarkable events because of their properties. Sometimes is for the exceptional value of some of the parameters listed above, others due to the observation of a new effect for the first time. A list of the most noticeable binary systems divided by catalog is visible in Table 1. Note that while they are defined as confident, for some of them the actual origin is still uncertain.

CATALOGS	SOURCES
GWTC-1	- GW150914 : first detection of gravitational waves from the merger of two black holes - GW170729 : most massive event of the catalog with a total mass of $\sim 84\,\mathrm{M_\odot}$ - GW170817 : first detection of a binary neutron star merger (BNS) - GW170814 : first signal measured with three detectors - GW170818 : only event of the catalog not being either face-on or face-off, with $45° < \theta_{JN} < 135°$.

CATALOGS	SOURCES
GWTC-2	- GW190521: BBH with a total mass of $\sim 150\,\mathrm{M}_\odot$, most massive event - GW190924_021846 : least massive system with $m_2 > 3\,\mathrm{M}_\odot$ - GW190814 : potentially NSBH, it has the smallest mass ration of all the candidate events of the catalog with $q \sim 0.112$ - GW190425 : masses of the objects compatible with those of NSs - GW190514_065416 : event with the smallest effective spin, $\chi_{eff} \sim -0.19$ - The BBH with the largest Effective spin measure are GW190517_055101 ($\chi_{eff} \sim 0.5$) and GW190719_215514 ($\chi_{eff} \sim 0.3$) - GW190412 : this is the only case with mild evidence of precession
GWTC-2.1	- GW190426_190642 : event with the biggest total mass since now $M \sim 182\,\mathrm{M}_\odot$ - GW190917_114630 : component masses consistent with NSBH - GW190403_051519 : most extreme effective spin measured since now $\chi_{eff} \sim 0.89$ - GW190403_051519 and GW190917_051519 : most asymmetric signal detected, both have $q \sim 1/5 \sim 0.2$

CATALOGS	SOURCES
GWTC-3	- GW191219_163120 : compatible with a NSBH event, it has the smallest mass ratio measured $q \sim 0.038$ - GW191129_134029 : lowest BBH system detected in the catalog with $M \sim 17\,\mathrm{M}_\odot$ - GW200220_061928 : is the candidate with the highest mass of the third catalog with a mass of $M \sim 148\,\mathrm{M}_\odot$ - GW191109_010717: candidate event with the lowest effective spin measured since now $\chi_{eff} \sim 0.29$ - GW200308_173609 and GW200208_222617 have the highest positive effective spin, respectively of $\chi_{eff} \sim 0.45$ and $\chi_{eff} \sim 0.65$ - GW200129_065458 and GW191219_16312 are possible candidate to be edge-on

Table 1: List of significant events detected in each catalog

3 Binary Black Holes Population Properties

Combining the information about the population of sources detected, one can identify some trends that can help to understand more things about the binary formation and the characteristics of these astrophysical objects.

Using the data provided by the LIGO-Virgo-KAGRA collaboration [2] we did some studies about the compact binary systems distribution in the parameters space, in order to find still undetected combinations of them. Then we compared the conclusions with what was inferred by the collaboration in their studies of the population properties [6] [12] [13]. Since the noise of the detector impairs the measurements and the number of sources we currently have is not statistically significant, it is challenging to draw a firm conclusion by now.

3.1 Confidently detected events

Only the confident detections found in the GWTC will be taken into account for the analysis that follows. These are events with $p_{\mathrm{astro}} > 0.5$ and since there is no threshold for the FAR, is expected that around $\sim 10 - 15\%$ of candidates are originated by instrumental noise fluctuations. [13]

Note that in this paragraph Final Mass and Redshift are not represented because they are proportional respectively to the Total Mass and the Luminosity Distance (see Appendix A). To include them would have led to a redundancy in the results.

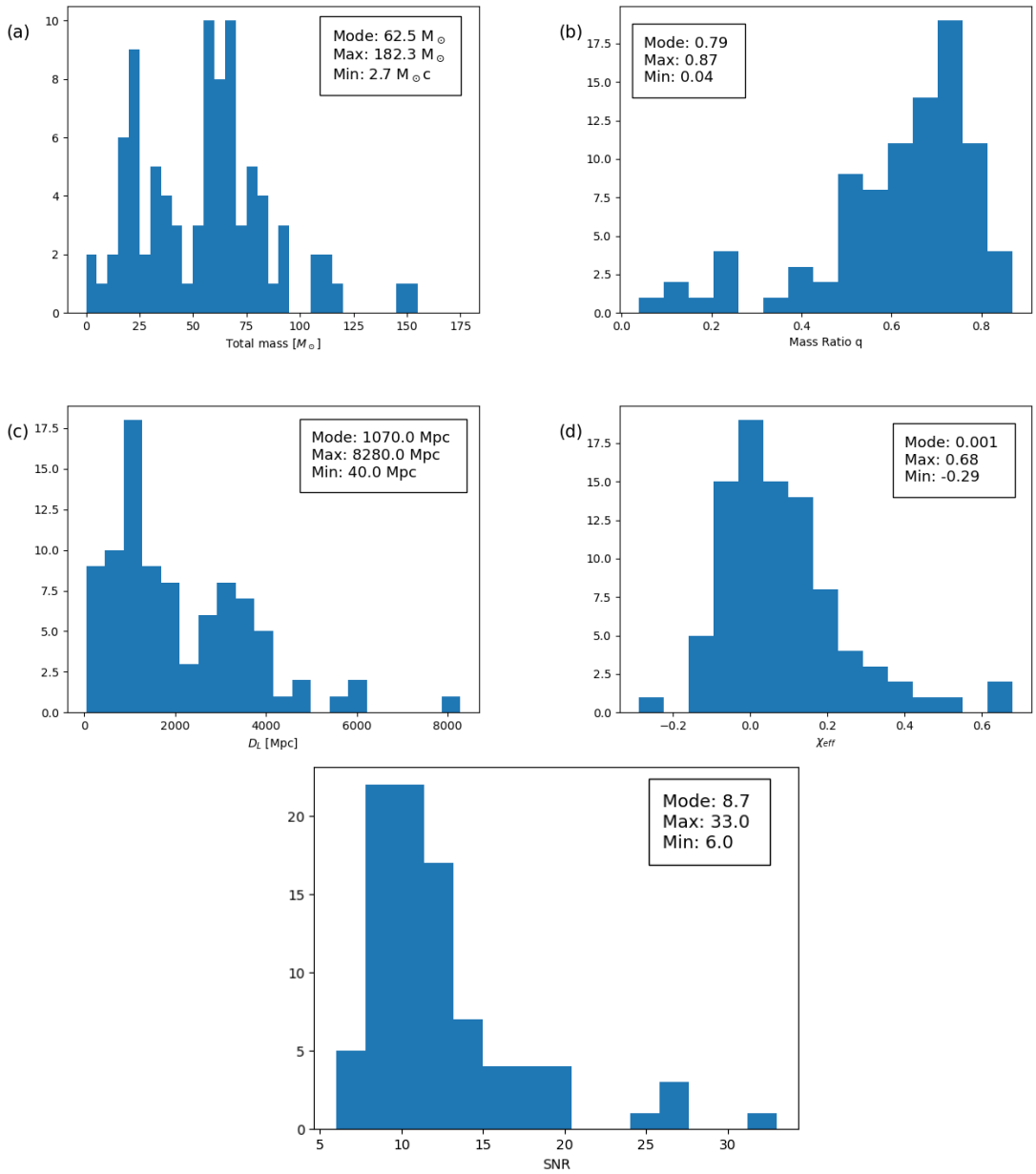

Figure 3: Histograms showing the main inferred properties of binary systems detected through gravitational waves, each one has reported the mode (the most frequent value), maximum value, and minimum value. Panel (a) shows the Total Mass M, panel (b) the Mass Ratio q, panel (c) the Luminosity Distance D_L, panel (d) the Effective Spin χ_{eff} and panel (e) SNR.

3.1.1 Parameters Distribution

We first plotted a histogram for each parameter to observe their distribution, identifying the maximum and minimum values and the most frequent value (the mode).

The first interesting result is the distribution of the Total Mass M. From Figure 3 panel (a) it is possible to see that there are some small masses due to the binary neutron stars followed by two peaks, one around $25\,M_\odot$ and the other around $75\,M_\odot$. Above $60\,M_\odot$ the frequency lowers significantly, indicating the presence of just a few massive binary systems. It is likely that the first peak is due to the NSBHs systems.

Another interesting parameter is the mass ratio q and in particular, it can be seen

from the histogram in Figure 3 panel (b) that the majority of the events have high values of q, as expected. But at the same time there are no cases of full symmetry, where the ratio is exactly one, the biggest observed up to now is $q \sim 0.87$. Most of the values are between $0.4 < q < 0.8$, and there are just a few asymmetrical binary systems.

The Luminosity Distance D_L distribution is shown in Figure 3 panel (c). Most of the events measured have a short distance $D_L < 4000\,\mathrm{Mpc}$, which is in agreement with the fact that the amplitude of the gravitational waves is inversely proportional to the distance, only the larger masses can be detected from great distances.

For what concerns the Effective Spin χ_{eff}, the most frequent bin is around zero as visible from panel (d) of Figure 3. This indicates that the majority of the events have spins almost aligned with the angular momentum of the system. Although there are few extreme cases in both the negative and positive range, the distribution is mostly shifted towards positive values.

Lastly in panel (e) of Fig. 3 we can see the SNR distribution. Most of the values are generally below 20, but there are some outliers at higher values.

3.1.2 Parameters Correlation

We now plot the correlation between each of the most significant parameters (see Figure 4). It can be seen that certain events have distinct colours, this is done to help identify the relevant candidates of each catalog giving their dominant property, as shown in the legend.

In the first panel of Figure 4 is displayed the Mass 1 and Mass 2 correlation. Most of the events of the plot lie on the diagonal indicating that generally the slope, and then the ratio, is constant for all the binary systems. This is supported by the histogram previously examined, as well as by the graph in Panel (b) of Figure 4, showing the correlation between Total Mass and Mass Ratio. In the former, we can observe indeed that the binary systems with small values of q are just a few, limited mostly to candidates with low Total Mass, typically NSBHs.

It is also interesting to look at the Chirp Mass. Plotting $\mathcal{M}$ with respect to the Total Mass it is possible to verify the equation 2.2. We can observe in fact how the points exactly lie on the lines based on their particular ratio if we choose a few different values for q.

Looking at the Luminosity Distance vs. Total Mass plot in Panel (c) of Fig. 4 there are two interesting observations that we can draw. Both the lack of small sources at great distances and the absence of massive sources a small distances are visible. Mass 1 and Mass 2 exhibit a similar pattern.

Instead, in the last panel of Figure 4, we can observe how the Effective Spin and the Total Mass relate. Also in this case there is a consistent pattern: all the events have a χ_{eff} mean value around zero as expected, but the smaller events have smaller spins compared to the one more massive, that are more widely distributed.

3.2 Marginal events

For studying the correlation between parameters, one can consider both marginal and confident detections. In particular marginal events are those that have a $p - astro < 0.5$ but $FAR < 2yr^{-1}$

If we perform again the previous analysis using the complete list it is possible to see that all the identified trends are confirmed. There are no significant outliers in

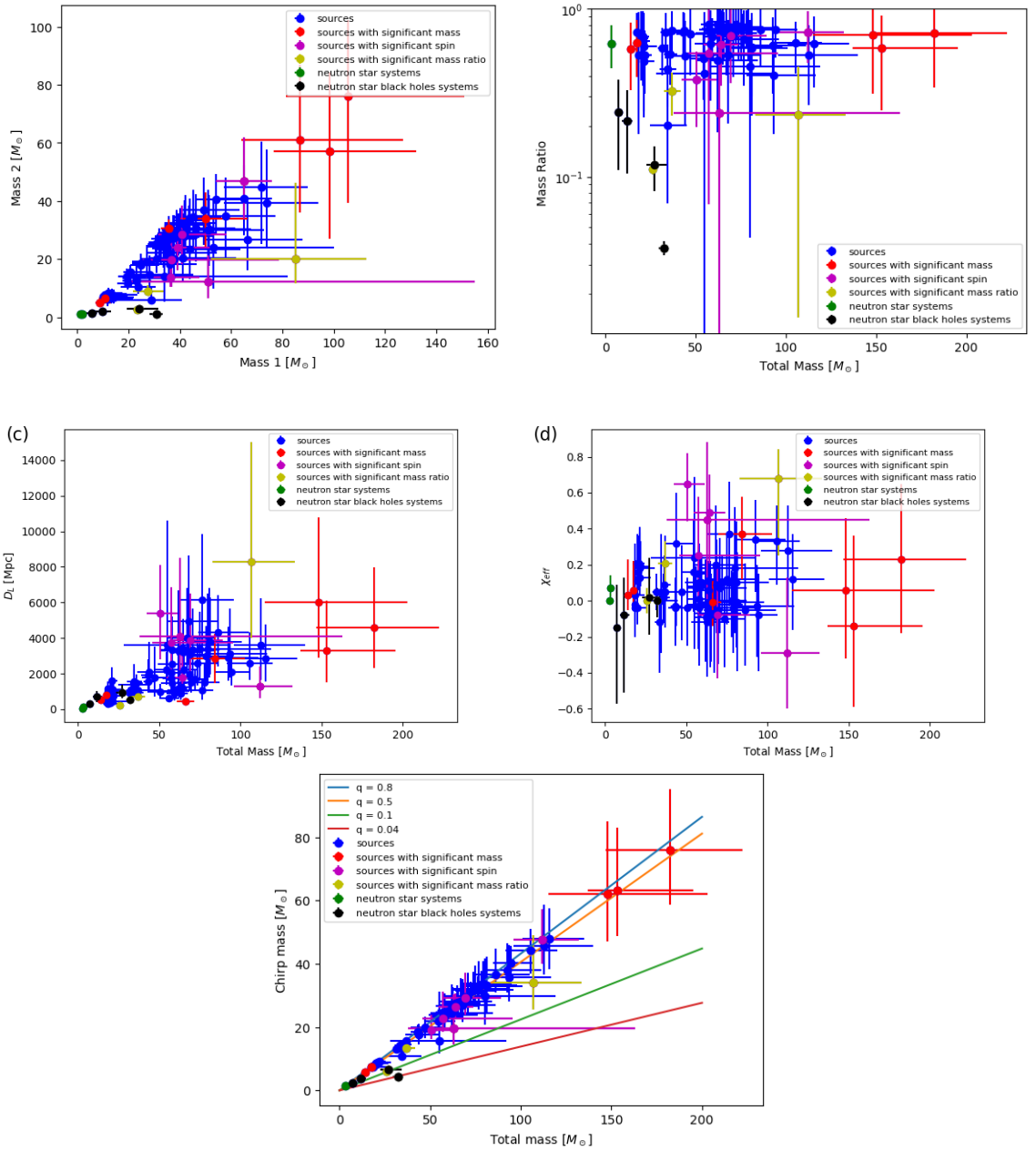

Figure 4: Plots showing the correlations between different parameters of the binary systems detected through gravitational waves. Panel (a) shows the distribution of Mass 1 with respect to Mass 2. Instead the other panels show the correlation between the Total Mass and Mass Ratio (b), Luminosity Distance (c), Effective Spin χ_{eff} (d) and Chirp Mass $\mathcal{M}$ (e).

the population, practically all the new events are located in the currently populated regions.

3.3 Results Interpretation

The LIGO-Virgo Collaboration also conducted a similar analysis and published their results in the cited papers. [6] [12] [13] The purpose of this paragraph is to compare their conclusions with what we have observed previously. It is important to emphasise that only Black Holes events with a FAR $< 1\text{yr}^{-1}$ have been taken into account, including some present in Table 1

The distribution of mass and spin enables us to understand more about the formation processes of compact objects, where the two main formation scenarios proposed by the scientists are the **isolated binaries evolution** ("in-the-field") and **dynamical formation**. The former channel involves binaries evolving together from pairs of massive stars into black holes or neutron stars. Instead in the dynamical formation, neutron stars and black holes become a binary after their formation in dense environments such as globular clusters or nuclear star clusters.[10]

Regarding the mass, the first important observation is the presence of two mass gaps. The first one, also referred to as the **Lower Mass Gap**, is situated between the heaviest NSs and the lightest BHs, in the range of $3\,M_\odot$ and $5\,M_\odot$. It is likely caused by the physics of the core-collapse supernova explosions, but due to the significant uncertainties in the estimation of the masses, it is not yet fully constrained. [13]. It is possible to observe the presence of this gap in our plot by zooming around the interested area in panel (a) of Figure 4, where we can see that there is no event in the zone delimited by the lines, except the error bar of a NSBH event. At the same time, if we look at the distribution of Mass 1 using a histogram, we can see a dearth just below $10\,M_\odot$ not clearly visible in the case of Total Mass. Both these plots are shown in Fig. 5.

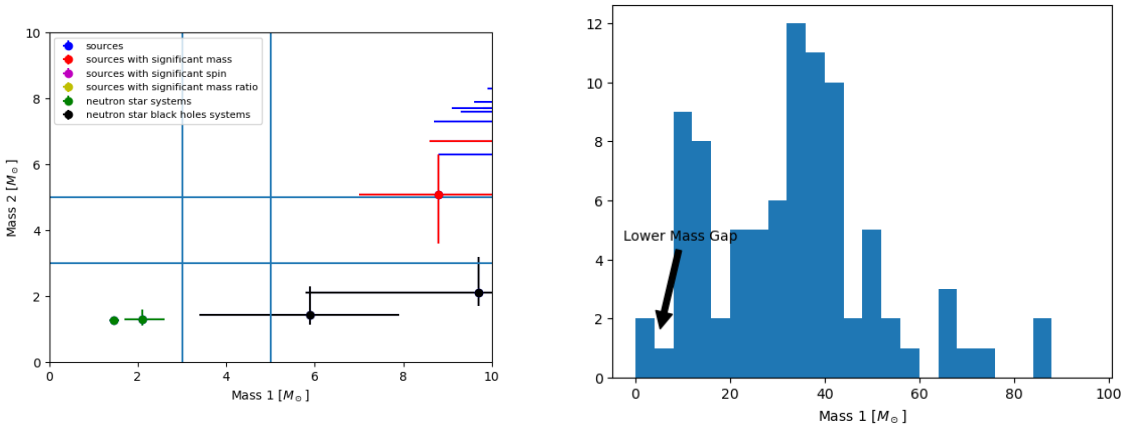

Figure 5: In this plot is shown a mild evidence of the presence of the lower mass gap. On the left, through the correlation of Mass 1 and Mass 2, on the right with the histogram of Mass 1.

The second gap, or **Upper Mass Gap**, between $50\,M_\odot$ and $120\,M_\odot$ is predicted by the stellar evolution models. This is caused by a specific type of supernova, the pulsational pair-instability supernovae. At this time the analysis of the full catalogue provides no evidence of the presence of this gap, all the results are inconclusive. Not even in our previous plots can be identified. A possible explanation is the presence of stars formed through hierarchical mergers under a dynamical formation scenario when a remnant of a previous merger encounters another compact object merging again. Alternatively, binaries in gaseous environments tend to gain mass through gas absorption. [10]

The existence of the Malquist Bias is another significant phenomenon to consider. The signal of more massive objects has a bigger amplitude and since the loudness of the signal decreases with the distance, it is possible to detect them even at large distances. This is probably the reason for the lack of small sources at big distances pointed out before in Section 3.1.2.

If we focus now on Effective Spin it is important to know that usually the spin of binaries formed in isolated environments is more aligned with the orbital axis,

compared to the one formed from a dynamical environment, that is isotropically oriented. [10] Because of this the presence of non-zero spin events is a strong indicator of the existence of a dynamically formed population of black holes, which should also yield to precession. [14] The Effective Spin distribution inferred is small but nonvanishing, with a mean value of $0.06^{+0.04}_{-0.05}$ however, the spins are larger and more dispersed in the heaviest masses. Conclusions that are also supported by the astrophysical model predictions [13] and are consistent with the previously reported plots. Unfortunately, the trend is well constrained just for small masses, there are not enough massive events to support this. [13].

In [13] is also noted an anti-correlation between the mass ratios and the spin. This means that binaries with an unequal mass ratio should prefer a more positive χ_{eff}, compared to the cases with $q \sim 1$, that have spins usually consistent with zero [13]. Therefore this pattern is not qualitatively evident in our data, as one can see in Fig 6.

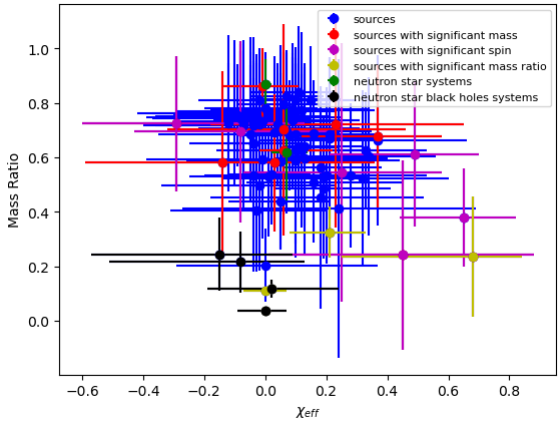

Figure 6: Correlation between Mass 1 and Effective Spin of detected sources. It shows no sign of anti-correlation among the two parameters.

4 Yet-undetected sources

Based on the prior observations it is possible to identify a list of interesting characteristics not yet detected in sources. For each set of parameters, one can make a time domain simulation and then a Fast Fourier Transform. From the former, we can also derive the Amplitude Spectral Density (ASD) and compare it with the sensitivity curve of the three detectors expected during O5 (see Figure 7. Doing so we can examine the features of the signal of that particular source and its detectability. This can be computed through the python py-CBC waveform module [4] [1]

For doing the simulations the parameters of the binary systems we have to set in the code are the masses of the two components, the Luminosity Distance, the inclination angle, and the individual spin components. However, we decided to constrain the Total Mass M and the Mass Ratio q instead of the single component masses. And for the spin, we made a further hypothesis of equal spin oriented along the z-axis, in order to determine the proper Effective Spin χ_{eff}. The starting frequency of the waveform is set at 20 Hz.

Note that the values of the parameters that we are not interested in are set around the value that occurs the most frequently for each binary system under study.

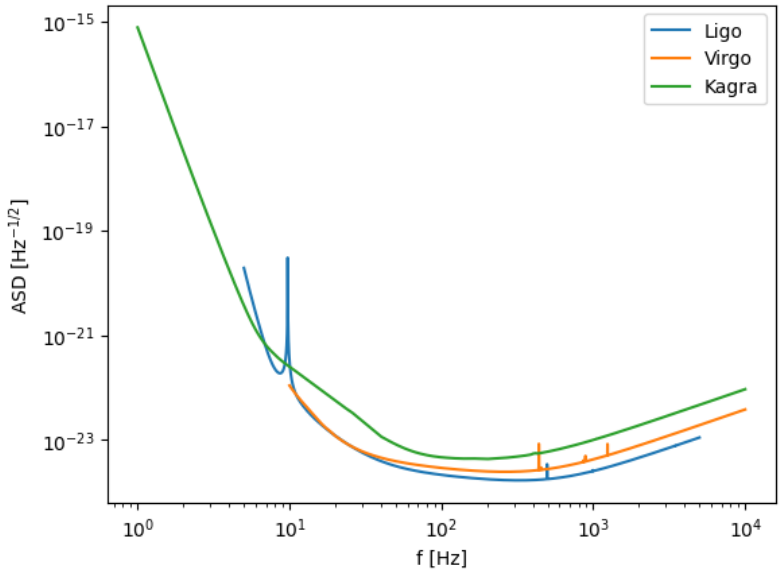

Figure 7: In this Figure is displayed the expected sensitivity curve of the three detectors during the O5 run.

4.1 Symmetry of the system

The first parameter we considered is the mass ratio. This distribution is particularly interesting because most of the events only span a narrow interval. In fact, as we have previously settled in Section 3.1.1 observing Fig. 3, the majority of the detected events are symmetric, with a mass ratio $q \sim 0.8$. Due to this, we made two simulations of the two extremes: an asymmetric source with $q \sim 0.02$, which value is smaller than anything we detected up to now, and the other of a completely symmetric source with $q = 1$. The set of example parameters we used is:

$$\text{(1A) M} = 102\,\mathrm{M}_\odot, \quad \text{q} = 0.02, \quad D_L = 900\,\mathrm{Mpc}, \quad \chi_{eff} = 0, \quad \theta_{JN} = 0$$

$$\text{(1B) M} = 100\,\mathrm{M}_\odot, \quad \text{q} = 1, \quad D_L = 900\,\mathrm{Mpc}, \quad \chi_{eff} = 0, \quad \theta_{JN} = 0$$

The result of the simulation is shown in Figure 8.
It is very remarkable to see how just changing the mass ratio of the source both the amplitude and the frequency of the signal change. In particular, the signal of the asymmetric binary system is smaller, probably leading to more difficulties in the measurement. The reason for the absence of asymmetric sources then could lie in a detection problem, and not in a real lack of these events. However, it seems that thanks to the sensitivity curves we will reach in O5, asymmetric candidates are more easily detectable at this distance. At the same time, there seems to be no reason for an absence of sources with $q = 1$ looking at the simulation, in this case the cause can be sought in the process of binary formation.

4.2 Total Mass and Distance correlation

Another peculiar pattern we observed in Figure 4 is the lack of sources with high total mass at short distances and sources with low total mass at great distances. It is therefore worthy to study both these cases using two example sources with the following parameters:

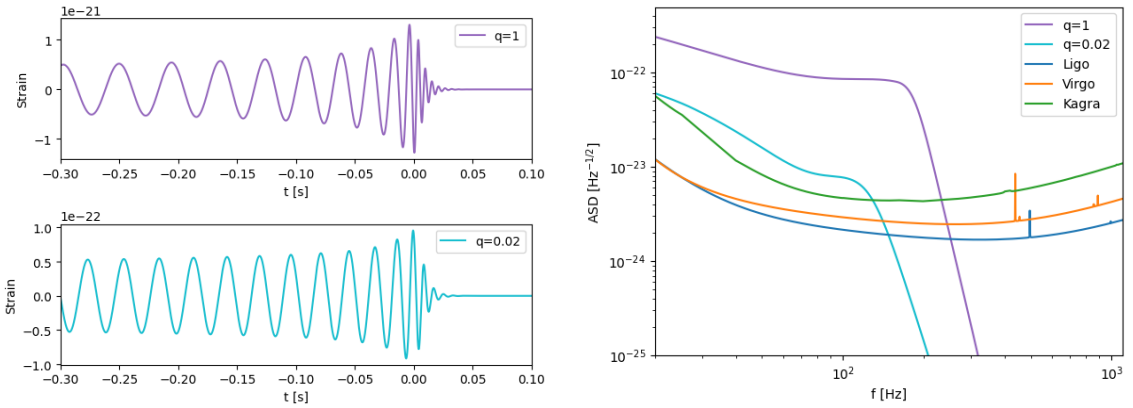

Figure 8: This plots are the results of a simulation for two yet undetected sources of interest. They show the time domain signal on the left, and the Amplitude Spectral Density on the right, of two binary systems with respective mass ratios $q = 0.02$ and $q = 1$.

$$\text{(2A) } \mathrm{M} = 170\,\mathrm{M}_\odot, \quad \mathrm{q} = 0.7\ , \quad D_L = 400\,\mathrm{Mpc}, \quad \chi_{eff} = 0, \quad \theta_{JN} = 0^\circ$$

$$\text{(2B) } \mathrm{M} = 34\,\mathrm{M}_\odot, \quad \mathrm{q} = 0.7, \quad D_L = 6000\,\mathrm{Mpc}, \quad \chi_{eff} = 0, \quad \theta_{JN} = 0^\circ$$

The corresponding time domain signal and ASD obtained through the simulation are displayed in Figure 9.

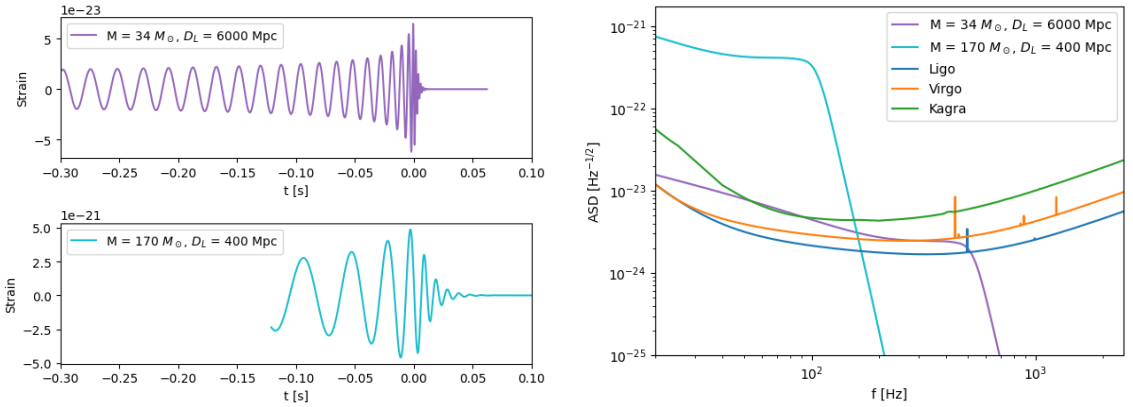

Figure 9: This plots are the results of a simulation for two yet undetected sources of interest. They show the time domain signal on the left, and the Amplitude Spectral Density on the right, of two binary systems with respective high mass and short distance, and low mass and large distance.

From these plots, one can see how the source (2A) has higher frequencies but smaller amplitudes. This is expected because the amplitude of the signal scale with distance and the frequency of rotation of a binary system is inversely proportional to its mass. It is interesting to note that such a small amplitude can make it impossible to detect this kind of source, in agreement with the observed Malmquist Bias discussed in Section 3.3. However, with this specific set of parameters, and with the sensitivity expected by O5 it seems that (2A) can be detected if we don't consider noise, at least by LIGO. Therefore, in order to solve this bias for the future the sensitivity of the detector should be increased. On the other hand, signal (2B) is very loud and

detectable, so the reason for this absence probably lies in some astrophysical process that disfavors this kind of source.

Another interesting unobserved source absent in Figure 4 is a binary system with high mass and large distance. This can be compared with another source that has the same mass but is closer.

$$\text{(2C) M} = 190\,\mathrm{M}_\odot, \quad \text{q= 0.72}, \quad D_L = 10.000\,\mathrm{Mpc}, \quad \chi_{eff} = 0, \quad \theta_{JN} = 0°$$

$$\text{(2D) M} = 190\,\mathrm{M}_\odot, \quad \text{q= 0.72}, \quad D_L = 400\,\mathrm{Mpc}, \quad \chi_{eff} = 0, \quad \theta_{JN} = 0°$$

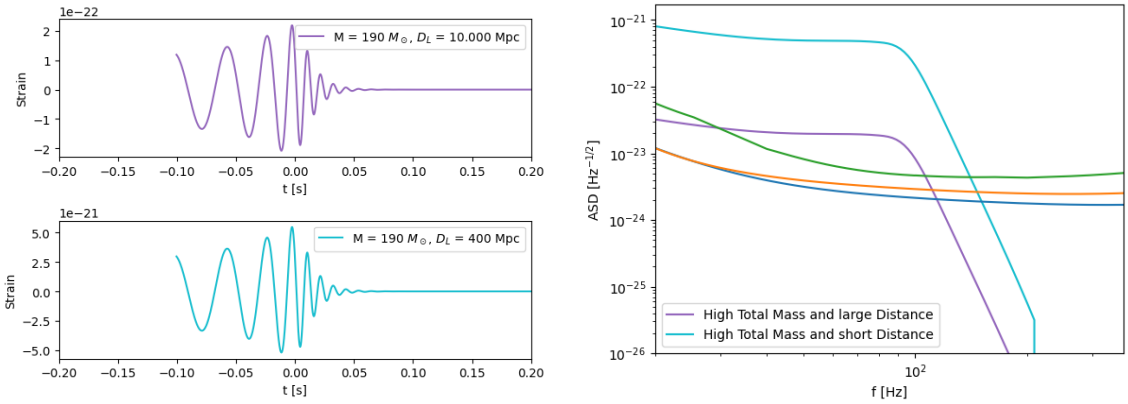

Figure 10: This plots are the results of a simulation for two yet undetected sources of interest. They show the time domain signal on the left, and the Amplitude Spectral Density on the right, of two binary systems with respective high mass and short distance, and high mass and large distance.

Looking at the plot in Figure 10 one can see how the shape of the two signals is exactly the same, but it changes only the amplitude, for the reasons explained above. It is also clear that the source (2C) is more easily detectable than (2A), therefore if such a source exists we will likely be able to see it in the next run.

4.3 Total Mass and Effective Spin correlation

We already discussed in Section 3.3 how small masses have a lower spin, and for higher masses the effective spin distribution is more spread. We said that this is because of to the formation history of these objects: binaries born from isolated stellar evolution have aligned spins, on the contrary binaries with a dynamical formation have an isotropic orientation of spins.

Therefore an example of undetected sources is two low-mass systems, one with a high positive Effective Spin and the other with a high negative Effective Spin. The example parameters chosen for this simulation are:

$$\text{(3A) M} = 36\,\mathrm{M}_\odot, \quad \text{q} = 0.8, \quad D_L = 900\,\mathrm{Mpc}, \quad \chi_{eff} = 0.9, \quad \theta_{JN} = 0°$$

$$\text{(3B) M} = 36\,\mathrm{M}_\odot, \quad \text{q} = 0.8, \quad D_L = 900\,\mathrm{Mpc}, \quad \chi_{eff} = \text{-}0.9, \quad \theta_{JN} = 0°$$

The simulation results are shown in Figure 11, where we plotted together the two time-domain signals to emphasise the differences.

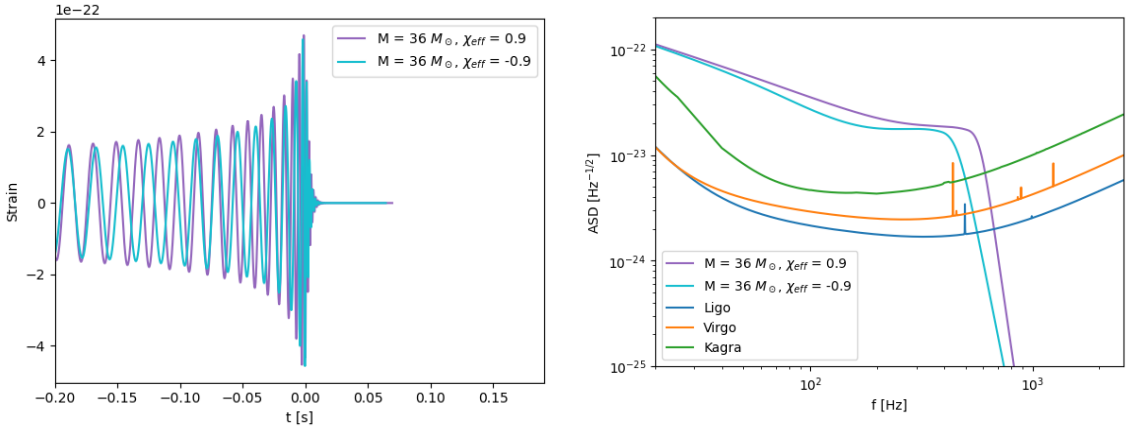

Figure 11: This plots are the results of a simulation for two yet undetected sources of interest. They show the time domain signal on the left, and the Amplitude Spectral Density on the right, of two low Total Mass binary systems with high Effective Spins but opposite sign

It is interesting to note how the difference between the two signals is small, making it harder to discern a positive spin from a negative spin. One can also wonder what changes if we consider a higher mass. Changing the mass the parameters become:

$$\text{(3C) M} = 135\,\mathrm{M}_\odot, \quad \text{q} = 0.8, \quad D_L = 900\,\mathrm{Mpc}, \quad \chi_{eff} = 0.9, \quad \theta_{JN} = 0^\circ$$

$$\text{(3D) M} = 135\,\mathrm{M}_\odot, \quad \text{q} = 0.8, \quad D_L = 900\,\mathrm{Mpc}, \quad \chi_{eff} = \text{-}0.9, \quad \theta_{JN} = 0^\circ$$

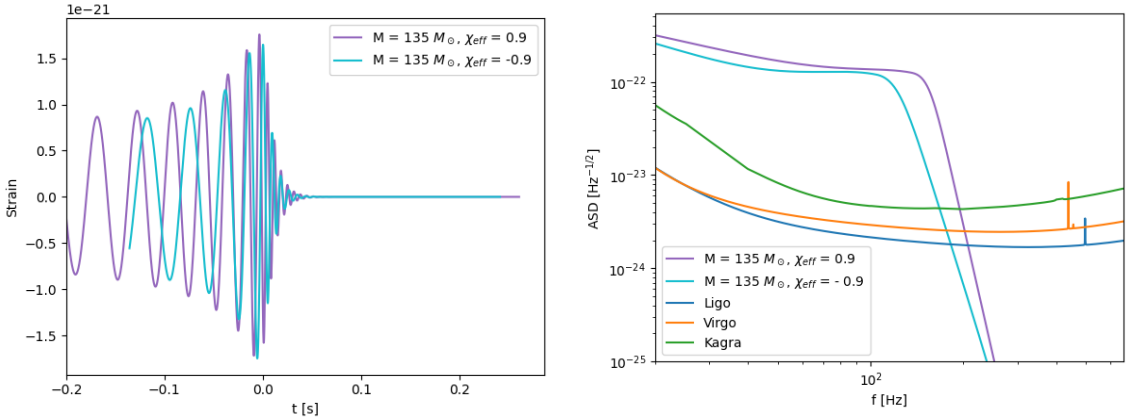

Figure 12: This plots are the results of a simulation for two yet undetected sources of interest. They show the time domain signal on the left, and the Amplitude Spectral Density on the right, of two high Total Mass binary systems with high Effective Spins but opposite sign

Comparing the right panel of Figure 12 and Figure 11 one can see that since lower masses have higher frequencies, and the plot has a logarithmic scale on both axes, the difference is greater for higher masses. So for massive sources, it is easier to distinguish a positive Effective Spin from a negative one.

4.4 Inclination angle

The majority of the binaries observed so far are face-on ($\theta_{JN} = 0°$) or face-off ($\theta_{JN} = 180°$), with only a few cases showing signs of other inclination angles. (see Table 1)

One may attempt to simulate of how we would see the same system with different inclinations. The example sources used are:

$$\text{(4A) } \mathrm{M} = 70\,\mathrm{M}_\odot, \quad \mathrm{q} = 0.75, \quad D_L = 900\,\mathrm{Mpc}, \quad \chi_{eff} = 0, \quad \theta_{JN} = 0°$$

$$\text{(4B) } \mathrm{M} = 70\,\mathrm{M}_\odot, \quad \mathrm{q} = 0.75, \quad D_L = 900\,\mathrm{Mpc}, \quad \chi_{eff} = 0, \quad \theta_{JN} = 45°$$

$$\text{(4C) } \mathrm{M} = 70\,\mathrm{M}_\odot, \quad \mathrm{q} = 0.75, \quad D_L = 900\,\mathrm{Mpc}, \quad \chi_{eff} = 0, \quad \theta_{JN} = 90°$$

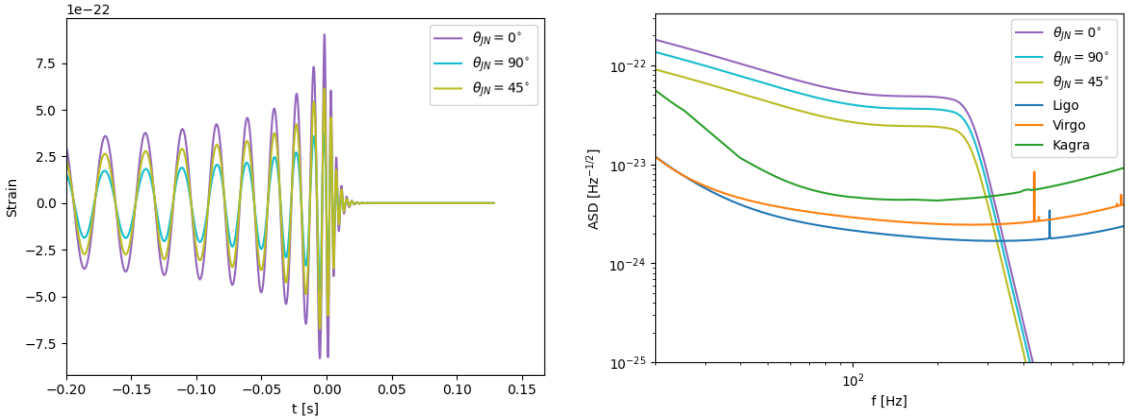

Figure 13: This plots are the results of a simulation for two yet undetected sources of interest. They show the time domain signal on the left, and the Amplitude Spectral Density on the right, of three low binary systems with different inclination angles.

In Fig. 13 are visible the signals obtained through the simulation. The only difference between the three signals' waveforms and ASDs is a small shift in amplitude. Moreover, the distance between the two extremes in the ASD is less than one order of magnitude. This may be one of the causes of the difficulties in the estimation of the Inclination Angle.

Additionally, we can also study the case of an asymmetric source with various inclination angles. This allows us also to check whether (2A) can also be detected at an inclination angle of $\theta_{JN} = 90°$. From Fig. 14 it is possible to conclude that even for LIGO will be difficult in O5 to detect this kind of source.

$$\text{(4A) } \mathrm{M} = 102\,\mathrm{M}_\odot, \quad \mathrm{q} = 0.02, \quad D_L = 900\,\mathrm{Mpc}, \quad \chi_{eff} = 0, \quad \theta_{JN} = 0°$$

$$\text{(4C) } \mathrm{M} = 102\,\mathrm{M}_\odot, \quad \mathrm{q} = 0.02, \quad D_L = 900\,\mathrm{Mpc}, \quad \chi_{eff} = 0, \quad \theta_{JN} = 90°$$

It would be also interesting to observe the signal of a precessing source, but the code used for this work is not implemented for this phenomenon so it will not studied further here.

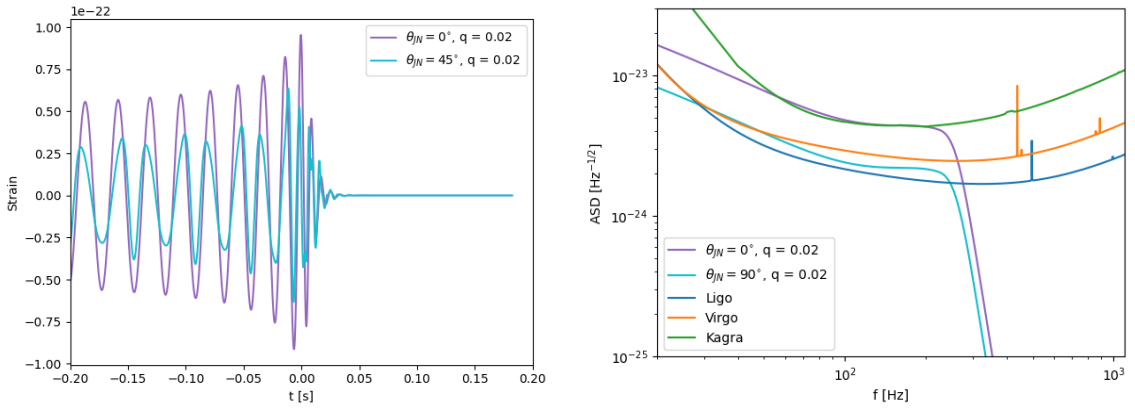

Figure 14: This plots are the results of a simulation for two yet undetected sources of interest. They show the time domain signal on the left, and the Amplitude Spectral Density on the right, of two asymmetric binary systems with different inclination angles.

5 Conclusions

While the number of detected gravitational wave events every day is growing, there are still many kinds of binary systems that we have not observed yet. Being aware of the characteristics of the already discovered events and preparing for upcoming observations could improve our capacity to identify the newly detected signals.

By looking at the data present in the GWTC-3, we studied the trends in the parameter spaces of the detected and yet-undetected events. In this report, the fundamental properties used to parametrize binary systems are: the Total Mass M, the Mass Ratio q, defined as the ratio of the higher and lower component mass, the Luminosity Distance D_L, the inclination angle between the line of sight and the orbital plane θ_{JN} and the Effective Spin χ_{eff}. The rest of this section summarizes our findings. Table 2 lists GW sources that have not yet been observed.

The distribution of the component masses is predicted to have two mass gaps. A Lower Mass Gap (3 - 5 $M_\odot$) between the more massive neutron stars and the lightest black holes, and a Higher Mass Gap (50 - 120 $M_\odot$). Our distributions do not show the latter, which can be explained by the hierarchical dynamical formation scenario. More GW events are needed to explore these gaps.

The majority of the detected binary systems seem to be symmetric, with a Mass Ratio around $q \sim 0.8$. It is partially caused by the smaller amplitudes of the waveforms from the asymmetric systems compared with the symmetric ones. Another reason is that asymmetric sources are more rare. With the detector sensitivity predicted for O5 these events will be easier to detect and we should prepare for this possibility. On the other hand, there is no reason to suppose that candidates with $q > 0.8$ (the maximum value observed) are prevented from being observed. Probably in this case, the cause lies in the astrophysical process of binary formation.

By looking at the distribution of the luminosity distance there are three main kinds of events not yet detected: both low mass and high mass at large distances, and close massive objects. The latter displays a very loud simulated signal, so the cause could be of astrophysical origin. Nonetheless, the first two have a smaller signal preventing them from being detected properly, for this reason, the best effort to increase detector sensitivity is needed. In particular, the absence of small masses from a certain distance is a known phenomenon labeled as Malmquis bias.

The candidates included in the catalogs usually have an Effective Spin distribution around zero, with evidence for a greater dispersion around the mean value for higher masses. By looking at the simulation of the waveform for high Effective Spin events, with low or high mass, it seems that the difference in the simulated spectra very small, and it is even smaller for the low mass binaries. This is important to keep in mind because it can cause problems in parameter estimation.

There is still no strong evidence of events with an inclination angle different from $\theta_{jN} = 0°$ and $\theta_{jN} = 0°$, but the simulations also show in this case a slight difference in the simulated amplitude between the various angles. Therefore it can be harder to distinguish between them.

In conclusion, there is still a lot of interesting events that can to be detected. Further improvement in the sensitivity of the interferometer is surely desirable. On the other hand, we recommend focusing future research mainly on a more detailed study of high mass ratio GW events and in trying to constrain better the Effective Spin and Inclination angle.

FUTURE POTENTIAL DISCOVERY EVENTS
- Binary systems with at least a component in the Lower Mass Gap (3 - 5 $M_\odot$) or the Higher Mass Gap (50 - 120 $M_\odot$)
- Largely asymmetric binary systems, with a small Mass Ratio
- Completely symmetric binary systems with $q > 0.8$
- Binary systems at large distances with large and small masses
- Close massive binaries
- Binary systems with various inclination angles

Table 2: Future potential discovery events

Appendix A Correlated parameters

In this report some of the listed parameters above have never been taken into consideration, but it is interesting to see how some of them are linearly dependent. Therefore talking about Final Mass is equivalent to discussing Total Mass, and Luminosity Distance is the same as Redshift, all it takes is just a shift in the axis of the plots. It can be seen in Fig. 15, where the correlation between the two parameters is shown, with the Pearson coefficient r. In both cases $r \sim 1$, indication of a strong correlation.

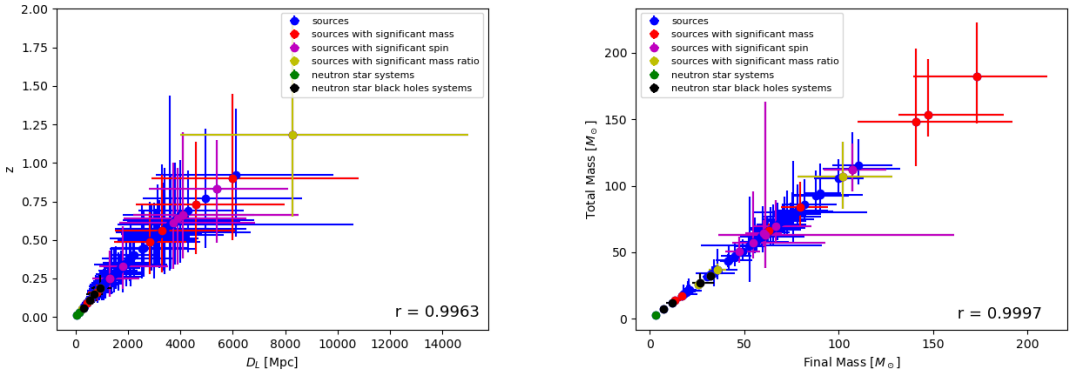

Figure 15: In this figure is displayed the correlation and the Pearson Luminosity Distance and Redshift on the left, Final Mass and Total Mass on the right.

References

[1] C. M. Biwer et al. "PyCBC Inference: A Python-based Parameter Estimation Toolkit for Compact Binary Coalescence Signals". In: *Publications of the Astronomical Society of the Pacific* 131.996 (Jan. 2019), p. 024503. DOI: 10.1088/1538-3873/aaef0b. URL: https://doi.org/10.1088%2F1538-3873%2Faaef0b.

[2] *GWOSC - Gravitational Waves Open Science Center, Event portal*. URL: https://gwosc.org/eventapi/.

[3] S. Klimenko et al. "Method for detection and reconstruction of gravitational wave transients with networks of advanced detectors". en. In: *Physical Review D* 93.4 (Feb. 2016), p. 042004. ISSN: 2470-0010, 2470-0029. DOI: 10.1103/PhysRevD.93.042004. URL: https://link.aps.org/doi/10.1103/PhysRevD.93.042004 (visited on 04/11/2024).

[4] Alex Nitz et al. *gwastro/pycbc: v2.2.2 release of PyCBC*. Version v2.2.2. Sept. 2023. DOI: 10.5281/zenodo.8340277. URL: https://doi.org/10.5281/zenodo.8340277.

[5] The LIGO Scientific Collaboration and The Virgo Collaboration. *Binary Black Hole Population Properties Inferred from O1 and O2*. 2018. URL: https://www.ligo.org/science/Publication-O2BBHPop/index.php.

[6] The LIGO Scientific Collaboration and The Virgo Collaboration. "Binary Black Hole Population Properties Inferred from the First and Second Observing Runs of Advanced LIGO and Advanced Virgo". In: (2018). DOI: 10.48550/ARXIV.1811.12940. URL: https://arxiv.org/abs/1811.12940 (visited on 09/14/2023).

[7] The LIGO Scientific Collaboration and The Virgo Collaboration. "GWTC-1: A Gravitational-Wave Transient Catalog of Compact Binary Mergers Observed by LIGO and Virgo during the First and Second Observing Runs". In: (2018). DOI: 10.48550/ARXIV.1811.12907. URL: https://arxiv.org/abs/1811.12907.

[8] The LIGO Scientific Collaboration and The Virgo Collaboration. "GWTC-2: Compact Binary Coalescences Observed by LIGO and Virgo During the First Half of the Third Observing Run". In: (2020). DOI: 10.48550/ARXIV.2010.14527. URL: https://arxiv.org/abs/2010.14527.

[9] The LIGO Scientific Collaboration and The Virgo Collaboration. "GWTC-2.1: Deep Extended Catalog of Compact Binary Coalescences Observed by LIGO and Virgo During the First Half of the Third Observing Run". In: (2021). DOI: 10.48550/ARXIV.2108.01045. URL: https://arxiv.org/abs/2108.01045.

[10] The LIGO Scientific Collaboration and The Virgo Collaboration. *GWTC-3, A THIRD CATALOG OF GRAVITATIONAL-WAVE DETECTIONS*. 2021. URL: https://www.ligo.org/science/Publication-O3bCatalog/flyer.pdf.

[11] The LIGO Scientific Collaboration and The Virgo Collaboration. "GWTC-3: Compact Binary Coalescences Observed by LIGO and Virgo During the Second Part of the Third Observing Run". In: (2021). DOI: 10.48550/ARXIV.2111.03606. URL: https://arxiv.org/abs/2111.03606.

[12] The LIGO Scientific Collaboration and The Virgo Collaboration. "Population Properties of Compact Objects from the Second LIGO-Virgo Gravitational-Wave Transient Catalog". In: (2020). DOI: 10.48550/ARXIV.2010.14533. URL: https://arxiv.org/abs/2010.14533.

[13] The LIGO Scientific Collaboration and The Virgo Collaboration. "The population of merging compact binaries inferred using gravitational waves through GWTC-3". In: (2021). DOI: 10.48550/ARXIV.2111.03634. URL: https://arxiv.org/abs/2111.03634.

[14] The LIGO Scientific Collaboration and The Virgo Collaboration. *The population properties of compact objects following LIGO/Virgo Run O3a*. 2020. URL: https://www.ligo.org/science/Publication-O3aPopulations/index.php.